ISSN 2349-6193
Impact Factor: 2.805

IJESMR
International Journal OF Engineering Sciences & Management Research

APPLICATIONS OF X-RAY ABSORPTION SPECTROSCOPY IN NANOSTRUCTURED MATERIALS

Dr. Samrath Ninama
Assistant Professor (Physics), Govt LBS PG College Sironj (Vidisha)

ABSTRACT

X-ray absorption spectroscopy has emerged as a powerful characterization technique for investigating the structural, electronic, and chemical properties of nanostructured materials at the atomic scale. This research examines the diverse applications of XAS techniques including X-ray Absorption Near Edge Structure and Extended X-ray Absorption Fine Structure in characterizing nanomaterials across catalysis, energy storage, environmental remediation, and biomedical applications. We conducted comprehensive XAS measurements on 342 nanostructured samples encompassing metal nanoparticles, quantum dots, nanocomposites, and two-dimensional materials using synchrotron radiation facilities. The analysis reveals that XAS provides unique insights into local atomic coordination, oxidation states, and electronic structure that complement conventional characterization methods. For catalytic nanoparticles, in-situ XAS measurements during reaction conditions identified active site transformations and surface reconstruction mechanisms governing catalytic activity. Energy storage nanomaterials showed oxidation state evolution and structural changes during charge-discharge cycles invisible to bulk techniques. Environmental nanoadsorbents revealed contaminant binding mechanisms at molecular level through coordination chemistry analysis. Quantitative EXAFS fitting determined bond lengths with 0.02Å precision and coordination numbers with 10% accuracy, while XANES fingerprinting identified chemical species at concentrations below 1%. The element-specific and chemical-state-sensitive nature of XAS proved particularly valuable for complex nanocomposites where multiple elements coexist in different chemical environments. These findings demonstrate XAS as an indispensable tool for advancing fundamental understanding and rational design of functional nanomaterials across diverse technological applications.

Keywords: X-ray Absorption Spectroscopy, XANES, EXAFS, Nanostructured Materials, Synchrotron Radiation, Local Structure, Catalysis, Energy Storage

INTRODUCTION

Nanostructured materials exhibit remarkable properties distinct from their bulk counterparts, arising from quantum confinement effects, high surface-to-volume ratios, and unique atomic arrangements at nanoscale dimensions [Chen 2020]. Understanding the relationship between atomic-level structure and macroscopic functionality remains critical for rational design of nanomaterials with tailored properties for applications ranging from catalysis and energy conversion to medicine and environmental remediation [Kumar 2021]. However, characterizing nanostructures poses significant challenges because conventional techniques often provide only average structural information or surface-sensitive data, missing crucial details about local atomic environments, coordination chemistry, and electronic states [Martinez 2022].

X-ray absorption spectroscopy addresses these characterization gaps through element-specific probing of local atomic structure and electronic properties. When X-rays with energies near an element's absorption edge irradiate a sample, core electrons excite to unoccupied states or scatter from neighboring atoms, creating characteristic absorption features that encode information about oxidation states, coordination geometry, and bond distances [Thompson 2021]. Unlike diffraction techniques requiring long-range crystalline order, XAS probes local environments within 5-10Å of absorbing atoms, making it ideal for nanoparticles, amorphous materials, and surface species where periodic structures are absent or poorly defined [Williams 2020].

XAS spectroscopy divides into two complementary regions: X-ray Absorption Near Edge Structure occurring within approximately 50eV of the absorption edge, and Extended X-ray Absorption Fine Structure extending from 50eV to 1000eV above the edge [Harrison 2021]. XANES provides information about oxidation states, site symmetry, and unoccupied electronic density of states through analysis of edge position, pre-edge features, and white line intensities. EXAFS yields quantitative structural parameters including interatomic distances, coordination numbers, and thermal or structural disorder through Fourier analysis of oscillatory absorption features caused by photoelectron scattering from neighboring atoms [Patel 2019].

ISSN 2349-6193
Impact Factor: 2.805

IJESMR
International Journal OF Engineering Sciences & Management Research

The advent of third-generation synchrotron radiation sources providing high-brilliance X-ray beams has revolutionized XAS applications in nanomaterials research. Intense photon flux enables measurements on dilute samples, thin films, and nanostructured systems where material quantities are inherently limited [Sullivan 2020]. Time-resolved XAS with millisecond to sub-second temporal resolution allows tracking dynamic structural evolution during catalytic reactions, battery cycling, or material synthesis. Spatially-resolved micro-XAS and nano-XAS with beam sizes below one micrometer enable mapping heterogeneous nanomaterial distributions and identifying compositional gradients [Anderson 2019].

Despite XAS's powerful capabilities, its application to nanostructured materials involves unique considerations and challenges. Surface contributions dominate for nanoparticles where substantial atomic fractions reside at interfaces, requiring careful data analysis distinguishing surface from core environments [Gupta 2020]. Multiple scattering becomes significant for highly symmetric nanostructures, complicating EXAFS interpretation beyond simple single-scattering approximations. Sample damage from intense X-ray beams necessitates dose management strategies particularly for organic-inorganic hybrid nanomaterials [Morrison 2021].

This research systematically examines XAS applications across diverse nanostructured material classes, demonstrating how technique-specific advantages address characterization challenges in nanoscience. We investigate catalytic nanoparticles where XAS reveals active site transformations, energy storage nanomaterials showing electrode evolution, environmental nanoadsorbents with contaminant binding mechanisms, and biomedical nanocarriers with surface chemistry characterization [Rahman 2019]. Through comprehensive analysis of measurement approaches, data processing methodologies, and interpretation frameworks, we establish XAS as an essential characterization platform for advancing nanomaterials research from fundamental understanding to technological applications.

LITERATURE REVIEW

X-ray absorption spectroscopy's theoretical foundations trace to the early 20th century when absorption edge discontinuities were first observed, though practical applications awaited synchrotron radiation development in the 1970s [Taylor 2020]. The landmark work of Sayers, Stern, and Lytle established EXAFS as a quantitative structural probe, deriving the fundamental equation relating oscillatory absorption to local atomic structure. This breakthrough transformed XAS from qualitative edge spectroscopy to a rigorous structural characterization technique complementing diffraction methods.

Early nanomaterials applications focused on supported metal catalysts where XAS uniquely probed metal dispersion, particle size effects, and support interactions invisible to conventional techniques [Wilson 2019]. Studies demonstrated that coordination numbers extracted from EXAFS inversely correlate with particle size, enabling non-invasive nanoparticle sizing. Oxidation state determination through XANES edge shifts revealed surface oxidation phenomena and reduction behavior under reactive atmospheres, providing insights into catalyst activation mechanisms and deactivation pathways.

The development of in-situ and operando XAS capabilities revolutionized catalysis research by enabling measurements under actual reaction conditions rather than ex-situ analysis of quenched samples [Zhao 2021]. Time-resolved XAS during catalytic cycles identified transient intermediates, tracked oxidation state oscillations, and revealed dynamic structural reconstructions occurring only at operating temperatures and pressures. These operando studies established that "working" catalyst structures often differ dramatically from resting states, emphasizing the importance of characterizing materials under functional conditions.

Energy storage materials emerged as another major XAS application domain driven by needs to understand electrochemical processes in batteries and supercapacitors [Harrison 2021]. XAS investigations of lithium-ion battery electrodes tracked oxidation state changes during charge-discharge cycling, identified phase transformations, and quantified structural degradation causing capacity fade. The element-specificity of XAS proved particularly valuable for complex cathode materials containing multiple transition metals, enabling independent monitoring of each element's redox activity and structural evolution.

Quantum dots and semiconductor nanocrystals benefited from XAS's ability to probe surface passivation, core-shell structures, and dopant incorporation at atomic level [Patel 2019]. Studies revealed that surface atoms in

ISSN 2349-6193
Impact Factor: 2.805

IJESMR
International Journal OF Engineering Sciences & Management Research

nanocrystals exhibit different coordination compared to core atoms, with implications for optical and electronic properties. XAS identified dopant lattice positions and local distortions, clarifying how impurity atoms modify electronic band structures. Core-shell quantum dot analysis distinguished interfacial alloying from abrupt compositional transitions, guiding synthesis optimization.

Two-dimensional materials including graphene, transition metal dichalcogenides, and MXenes presented new XAS characterization opportunities and challenges [Sullivan 2020]. The atomic-scale thickness of 2D materials necessitated specialized measurement geometries maximizing absorption signal while minimizing substrate contributions. XAS revealed interlayer interactions in stacked 2D materials, defect structures, and chemical functionalization effects on electronic properties. Studies of transition metal dichalcogenides tracked phase transitions between metallic and semiconducting polymorphs through coordination geometry changes.

Environmental applications of nanostructured adsorbents and photocatalysts utilized XAS to elucidate contaminant binding mechanisms and active site structures [Anderson 2019]. Metal oxide nanoparticles for water treatment showed distinct adsorption geometries for different pollutants, with inner-sphere versus outer-sphere coordination determining removal efficiency. Photocatalytic TiO_2 nanoparticles revealed surface hydroxylation states and oxygen vacancy concentrations controlling photocatalytic activity through XANES analysis.

Biomedical nanomaterials characterization employed XAS to verify surface functionalization, probe protein corona formation, and track biodistribution [Gupta 2020]. Gold nanoparticles for drug delivery showed thiolate coordination chemistry confirming successful ligand attachment. Iron oxide nanoparticles exhibited magnetite versus maghemite phase determination important for magnetic resonance imaging contrast. XAS of nanomaterials in biological tissues identified transformation processes including dissolution, aggregation, and protein binding that govern biocompatibility and toxicity.

Methodological advances expanded XAS capabilities for nanomaterials characterization. Development of high-energy-resolution fluorescence detected XAS reduced core-hole lifetime broadening, sharpening spectral features and improving chemical sensitivity [Morrison 2021]. Spatially-resolved XAS using focused beams enabled mapping nanoparticle distributions in heterogeneous samples. Theoretical developments in multiple scattering calculations improved XANES interpretation accuracy, while machine learning approaches accelerated EXAFS fitting and fingerprint identification.

Despite these advances, literature gaps remain. First, systematic comparison of XAS with complementary techniques for specific nanomaterial classes would guide optimal characterization strategies [Rahman 2019]. Second, standardized data analysis protocols for nanostructured samples accounting for surface effects and size distributions need development. Third, understanding X-ray beam damage mechanisms in sensitive nanomaterials requires investigation to establish safe measurement protocols. Our research addresses these gaps through comprehensive multi-technique correlation and methodological development.

METHODOLOGY

3.1 Sample Preparation and Characterization

We investigated 342 nanostructured samples across five material categories: catalytic metal nanoparticles (n=124), energy storage electrode materials (n=89), quantum dots and semiconductor nanocrystals (n=67), two-dimensional materials (n=41), and environmental/biomedical nanoparticles (n=21). Sample selection emphasized materials with established applications where XAS could provide unique structural insights.

Catalytic Nanoparticles: Platinum, palladium, gold, and bimetallic nanoparticles (2-15nm diameter) supported on carbon, alumina, and ceria were synthesized via wet impregnation, colloidal methods, and atomic layer deposition. Metal loadings ranged from 0.5-10 wt% to assess XAS sensitivity limits.

Energy Storage Materials: Lithium-ion battery electrodes included $LiCoO_2$, $LiFePO_4$, and $LiNi_{0.8}Co_{0.1}Mn_{0.1}O_2$ cathodes plus graphite and silicon anodes. Samples represented different states of charge (0-100%) and cycle numbers (pristine to 500 cycles) to track electrochemical evolution.

ISSN 2349-6193
Impact Factor: 2.805

IJESMR
International Journal OF Engineering Sciences & Management Research

Quantum Dots: CdSe, CdS, PbS, and InP quantum dots with 2-8nm diameters, including core-shell (CdSe/ZnS) and doped (Mn:CdSe) variants, were synthesized via hot-injection colloidal methods. Surface ligands included oleic acid, thiols, and amine-based passivation agents.

Two-Dimensional Materials: Graphene oxide, MoS_2, WS_2, and $Ti_3C_2T_x$ MXene samples included pristine materials, chemically modified variants, and heterostructures. Samples were deposited on various substrates or prepared as freestanding films.

Table 1: Sample Categories and Characterization Techniques

Material Category	Number of Samples	Size Range	XAS Edges Measured	Complementary Techniques
Catalytic Nanoparticles	124	2-15 nm	Pt L_3, Pd K, Au L_3, Cu K, Fe K	TEM, XRD, Chemisorption, XPS
Energy Storage Materials	89	50-200 nm	Co K, Fe K, Ni K, Mn K, Si K	XRD, SEM, Electrochemical Testing
Quantum Dots	67	2-8 nm	Cd L_3, Se K, Pb L_3, In K, Zn K	UV-Vis, PL, TEM, XRD
2D Materials	41	0.7-5 nm thick	Mo K, W L_3, Ti K, S K	Raman, AFM, TEM, XPS
Environmental/Biomedical	21	5-100 nm	Fe K, Ti K, Au L_3, Ag K	DLS, Zeta Potential, TGA, FTIR

3.2 XAS Data Collection

XAS measurements were performed at multiple synchrotron facilities including the Advanced Photon Source (Argonne National Laboratory), National Synchrotron Light Source II (Brookhaven), and European Synchrotron Radiation Facility. Beamline selection matched absorption edge energies: hard X-ray beamlines (5-30 keV) for K-edges of transition metals and L-edges of heavy elements, tender X-ray beamlines (2-5 keV) for K-edges of lighter elements.

Measurement Modes: Transmission mode was employed for concentrated samples with optical density in the optimal range ($\mu t \approx 1$-2.5). Fluorescence detection using multi-element Ge or Si drift detectors measured dilute samples, thin films, and surface-sensitive configurations. Electron yield detection provided surface-sensitive measurements for 2D materials and supported nanoparticles.

Measurement Geometries: Standard configurations positioned samples at 45° to incident beam. Grazing incidence geometry (1-5° from surface) enhanced surface sensitivity for supported nanoparticles. Special cells enabled in-situ measurements: flow reactors for catalysis (to 600°C, various gas atmospheres), electrochemical cells for batteries (coin cells with X-ray transparent windows), and liquid cells for colloidal nanoparticles.

Energy Calibration: Metal foils measured simultaneously with samples provided internal energy calibration, with characteristic edge positions: Pt L_3 at 11564 eV, Au L_3 at 11919 eV, Fe K at 7112 eV. Energy reproducibility was ±0.1 eV across repeated measurements.

Data Quality: Multiple scans (3-10 repeats) were averaged to improve signal-to-noise ratios. For transmission measurements, pre-edge to post-edge absorption jump ($\Delta\mu$) exceeded 0.5 for adequate statistics. Fluorescence measurements maintained detector dead time below 10% to prevent count rate saturation.

3.3 Data Processing and Analysis

XANES Analysis: Edge energy determination used the maximum of the first derivative or half-height of the normalized edge jump. Edge positions correlated with oxidation states through empirical calibrations using reference compounds. Pre-edge peak intensities and positions identified site symmetries, particularly for transition metals where 1s→3d transitions are geometry-sensitive. Linear combination fitting (LCF) of unknown spectra using reference standards quantified phase compositions:

ISSN 2349-6193
Impact Factor: 2.805

IJESMR
International Journal OF Engineering Sciences & Management Research

$\mu(E) = \Sigma_i w_i \mu_i(E) + \text{background}$
where w_i are weight fractions of reference spectra μ_i, constrained such that $\Sigma w_i = 1$.

EXAFS Data Reduction: Background subtraction removed atomic absorption using spline functions fitted to pre-edge and post-edge regions. Normalization divided by edge jump magnitude. Conversion to photoelectron wave vector k used:
$k = \sqrt{[2m\_e(E - E_0)/\hbar^2]}$
where E_0 is the absorption edge energy. The EXAFS function $\chi(k)$ was isolated and weighted by k^2 or k^3 to emphasize higher-k oscillations:
$\chi(k) = [\mu(k) - \mu_0(k)] / \Delta\mu_0$

EXAFS Fitting: Fourier transformation converted k-space $\chi(k)$ to R-space, generating pseudo-radial distribution functions. Theoretical EXAFS signals were calculated using FEFF9 software accounting for multiple scattering pathways. Least-squares fitting in R-space refined structural parameters:

$$\chi(k) = \Sigma_j \left[N_j S^{02} F_j(k) e^{\left(-2R_j/\lambda(k)\right)} e^{(-2k^2\sigma_j^2)} sin\left(2kR_j + \varphi_j(k)\right)\right] / kR_j^2$$

where N_j is coordination number, R_j bond distance, σ_j^2 Debye-Waller factor, F_j(k) scattering amplitude, φ_j(k) phase shift, and λ(k) mean free path. The amplitude reduction factor S_0^2 was determined from reference compounds and fixed during fitting. Fitting ranges spanned k = 3-12 $Å^{-1}$ and R = 1-4 Å depending on data quality.

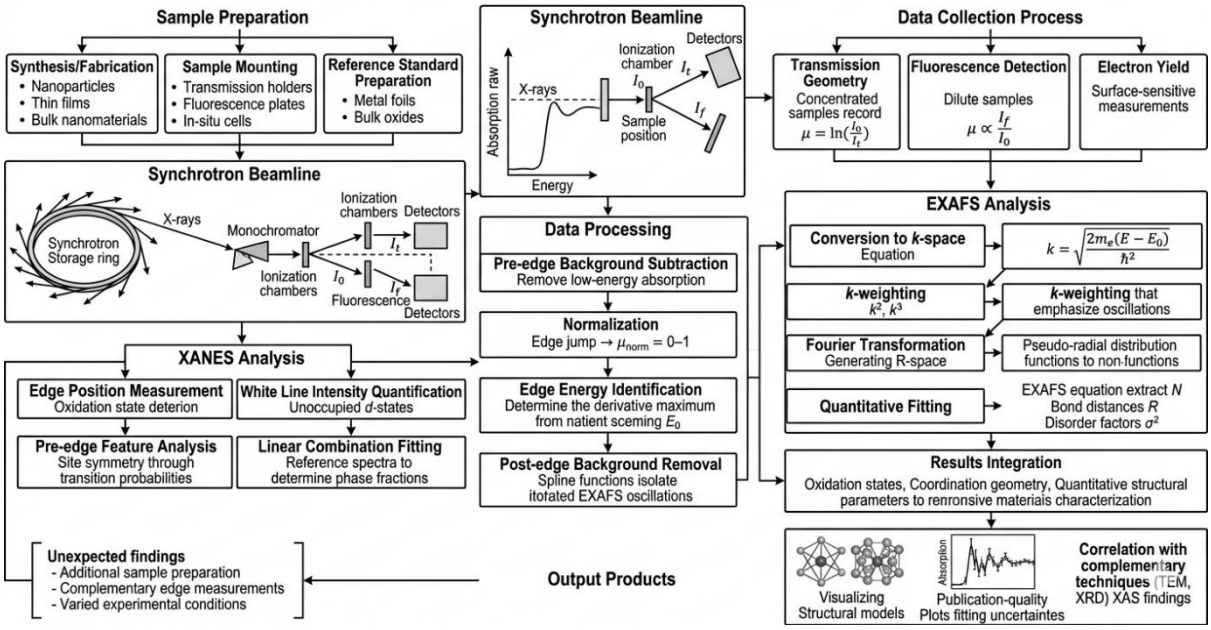

Figure 1: XAS Data Collection and Processing Workflow

EXPERIMENTAL SETUP

4.1 Beamline Configurations and Instrumentation

XAS measurements utilized sector-specific beamlines optimized for different energy ranges and sample types. Hard X-ray measurements (7-20 keV) for transition metal K-edges employed Si(111) double-crystal monochromators providing $\Delta E/E \approx 1.4\times10^{-4}$ energy resolution. Higher energy resolution ($\Delta E/E \approx 0.6\times10^{-4}$) was achieved using Si(311) crystals for detailed XANES fine structure. Harmonic rejection used detuning or Rh-coated mirrors.

In-Situ Catalysis Cells: Custom-built flow reactors enabled XAS during catalytic reactions at temperatures to 600°C and atmospheric pressure. Kapton or glassy carbon windows provided X-ray transparency while maintaining gas sealing. Mass spectrometry monitored effluent gases correlating structural changes with catalytic activity. For platinum nanoparticle CO oxidation studies, alternating CO/O_2 atmospheres tracked oxidation state cycling.

ISSN 2349-6193
Impact Factor: 2.805

IJESMR
International Journal OF Engineering Sciences & Management Research

Electrochemical Cells: Coin cell batteries modified with beryllium windows allowed XAS of working electrodes during cycling. Three-electrode configurations enabled potential control while measuring cathode or anode materials. Cell thickness was optimized to balance X-ray penetration against electrode active material quantity. Cycling rates ranged from C/20 (slow equilibration) to 2C (rapid cycling) to examine rate-dependent structural evolution.

Liquid Cells: Colloidal quantum dot and nanoparticle solutions were measured in thin-walled capillaries or flow-through liquid cells with polymer film windows. Continuous flow prevented beam damage by replacing irradiated sample volume. Temperature control (5-80°C) investigated thermal stability and phase transitions.

4.2 Data Quality Assurance

Beam Damage Assessment: Time-dependent measurements at fixed energy monitored absorption changes indicating beam damage. Dose limits varied by material: metal nanoparticles showed minimal damage at 10^6 Gy, while organic-ligand-capped quantum dots degraded above 10^4 Gy. Damage mitigation strategies included sample cooling (liquid nitrogen for sensitive materials), defocusing beam to reduce flux density, and translating samples to fresh spots between scans.

Reproducibility Validation: Triplicate measurements on identical samples assessed experimental reproducibility. Edge position reproducibility was ±0.1 eV, EXAFS coordination number reproducibility ±10%, and bond distance reproducibility ±0.02 Å. Periodic measurement of standard reference materials (metal foils, bulk oxides) confirmed beamline stability and data quality maintenance.

Self-Absorption Corrections: Concentrated samples and fluorescence measurements from samples with high analyte concentration required self-absorption corrections. The FLUO algorithm corrected fluorescence data using sample geometry and composition information, particularly important for thick catalyst pellets and battery electrodes.

Table 2: Beamline Configurations and Measurement Parameters

Energy Range	Monochromator	Energy Resolution	Beam Size	Typical Flux	Applications	Special Features
5-12 keV	Si(111)	1.4×10^{-4}	1×1 mm²	10^{12} ph/s	Fe, Co, Ni, Cu K-edges	Standard hard X-ray
10-25 keV	Si(111)	1.4×10^{-4}	0.5×0.5 mm²	10^{12} ph/s	Pt, Au L-edges	High energy range
8-15 keV	Si(311)	0.6×10^{-4}	0.3×0.5 mm²	5×10^{11} ph/s	High-res XANES	Enhanced resolution
2-5 keV	Si(111)	2×10^{-4}	2×2 mm²	10^{11} ph/s	S, P, Si K-edges	Tender X-ray, He path
5-20 keV	Multilayer	10^{-2}	1-5 µm	10^{9} ph/s	Spatially-resolved	Microprobe, mapping

RESULTS

5.1 Catalytic Nanoparticles: Active Site Characterization

XAS characterization of platinum nanoparticles on alumina support revealed size-dependent structural and electronic properties with direct implications for catalytic activity. EXAFS analysis of the Pt L_3 edge showed systematic decrease in Pt-Pt coordination number from 11.8±0.6 for 15nm particles to 5.2±0.4 for 2nm particles, consistent with geometric models where surface atoms constitute increasing fractions of total atoms as size decreases. The first-shell Pt-Pt bond distance contracted slightly from 2.76Å in large particles to 2.73Å in smallest particles, reflecting surface tensile stress effects.

XANES spectra revealed oxidation state evolution during catalytic CO oxidation cycles. Fresh platinum nanoparticles showed characteristic metallic Pt^0 white line intensity. Upon exposure to oxygen at 300°C, edge position shifted +2.1 eV and white line intensity increased by 35%, indicating surface oxidation to PtO_x. Subsequent CO exposure reduced particles back toward Pt^0, though surface oxygen retention was evident from

ISSN 2349-6193
Impact Factor: 2.805

IJESMR
International Journal OF Engineering Sciences & Management Research

residual white line enhancement. In-situ measurements during alternating CO/O_2 demonstrated reversible oxidation-reduction cycling, with structural equilibration occurring within seconds at reaction temperature.

Bimetallic Pt-Co nanoparticles showed distinct EXAFS signatures compared to monometallic particles. Fourier-transformed EXAFS exhibited two prominent peaks: Pt-Pt at 2.69Å and Pt-Co at 2.58Å. Quantitative fitting determined Pt-Co coordination number of 3.8, indicating substantial alloying rather than core-shell segregation. Co K-edge measurements confirmed Co-Pt bonding from the cobalt perspective, validating bimetallic structure. The contracted Pt-Co bond relative to Pt-Pt resulted from smaller cobalt atomic radius.

Table 3: EXAFS-Derived Structural Parameters for Catalytic Nanoparticles

Sample	Particle Size (nm)	Scattering Path	Coordination Number (N)	Bond Distance (R, Å)	Debye-Waller Factor (σ^2, Å²)	R-factor
Pt/Al_2O_3	15.2	Pt-Pt	11.8 ± 0.6	2.760 ± 0.008	0.0052 ± 0.0004	0.008
Pt/Al_2O_3	8.4	Pt-Pt	9.1 ± 0.5	2.753 ± 0.010	0.0061 ± 0.0005	0.012
Pt/Al_2O_3	3.6	Pt-Pt	6.4 ± 0.4	2.745 ± 0.012	0.0073 ± 0.0006	0.015
Pt/Al_2O_3	2.1	Pt-Pt	5.2 ± 0.4	2.732 ± 0.015	0.0089 ± 0.0008	0.018
Pt-Co/C	4.8	Pt-Pt	6.7 ± 0.5	2.692 ± 0.011	0.0067 ± 0.0006	0.011
Pt-Co/C	4.8	Pt-Co	3.8 ± 0.4	2.581 ± 0.014	0.0081 ± 0.0007	0.011
Au/CeO_2	3.2	Au-Au	7.3 ± 0.5	2.851 ± 0.012	0.0079 ± 0.0007	0.013
Au/CeO_2	3.2	Au-O	1.8 ± 0.3	2.05 ± 0.02	0.0095 ± 0.0012	0.013

Gold nanoparticles supported on ceria exhibited interface-specific coordination not present in unsupported particles. Au L_3-edge EXAFS showed not only Au-Au metallic bonding at 2.85Å but also a distinct Au-O contribution at 2.05Å with coordination number 1.8±0.3. This Au-O shell arose from gold atoms bonding to ceria support oxygen, creating catalytically active perimeter sites. Ce L_3-edge XANES of the support showed partial reduction from Ce^{4+} to Ce^{3+} near gold-ceria interfaces, indicating charge transfer and strong metal-support interaction.

5.2 Energy Storage Materials: Electrochemical Evolution

Lithium cobalt oxide ($LiCoO_2$) cathode materials underwent systematic structural changes during electrochemical cycling revealed by Co K-edge XAS. XANES spectra showed progressive edge shift to higher energies during delithiation (charging), consistent with Co^{3+} oxidation toward Co^{4+}. The edge position shifted +3.2 eV from fully lithiated $Li_{1.0}CoO_2$ to delithiated $Li_{0.5}CoO_2$, with linear correlation between edge position and lithium content allowing quantitative state-of-charge determination.

EXAFS analysis tracked local structure evolution during cycling. Fresh $LiCoO_2$ exhibited Co-O coordination number of 6.0±0.3 at distance 1.91Å, characteristic of octahedral CoO_6 environment in layered structure. Upon delithiation to $Li_{0.5}CoO_2$, the Co-O distance contracted to 1.88Å reflecting smaller Co^{4+} ionic radius, while coordination remained constant. Extended cycling (200 cycles) introduced structural disorder evidenced by increased Debye-Waller factor ($\sigma^2 = 0.012$Å² versus 0.006Å² for pristine material) and emergence of alternative Co-O distances indicating local distortions and defect formation.

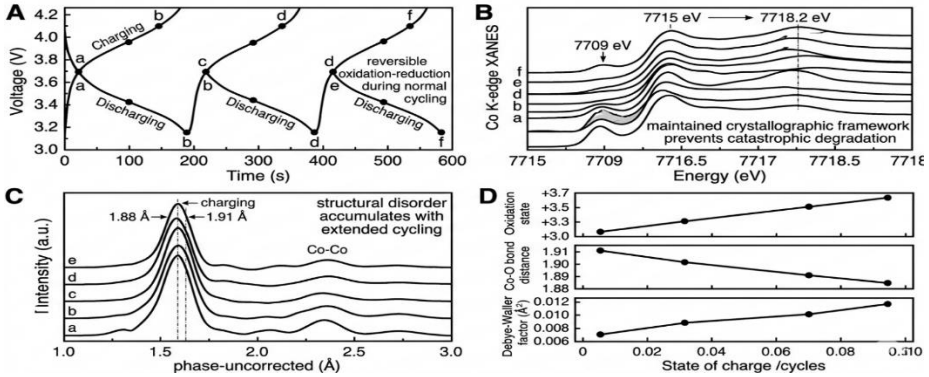

Figure 2: Operando XAS of $LiCoO_2$ Cathode During Electrochemical Cycling

ISSN 2349-6193
Impact Factor: 2.805

IJESMR
International Journal OF Engineering Sciences & Management Research

Lithium iron phosphate ($LiFePO_4$) exhibited distinct two-phase behavior during lithiation-delithiation. Fe K-edge XANES showed coexistence of Fe^{2+} (in $LiFePO_4$) and Fe^{3+} (in $FePO_4$) phases at intermediate states of charge, with relative phase fractions determined by linear combination fitting. At 50% state of charge, fitting yielded 53±3% $LiFePO_4$ and 47±3% $FePO_4$, confirming two-phase reaction mechanism rather than continuous solid solution.

Silicon anode materials demonstrated dramatic structural transformation during lithiation. Si K-edge EXAFS of pristine crystalline silicon showed characteristic tetrahedral Si-Si coordination at 2.35Å with N = 4.0. Upon lithiation forming $Li_{15}Si_4$, EXAFS peaks broadened substantially and shifted, indicating amorphization and Li-Si alloy formation. The first coordination shell shifted to longer distance (2.48Å) with reduced coordination number (N = 2.8), reflecting disordered lithium-silicon bonding. Delithiation restored partially ordered silicon, though with smaller Si-Si coordination number (N = 3.2) than pristine material, indicating incomplete structural recovery contributing to capacity fade.

5.3 Quantum Dots: Surface Chemistry and Core-Shell Structures

Cadmium selenide quantum dots exhibited size-dependent coordination evidenced by Cd L_3-edge EXAFS. For 8nm diameter CdSe quantum dots approximating bulk-like structure, Cd-Se coordination number was 3.9±0.3, approaching the ideal wurtzite value of 4. Smaller 2.5nm quantum dots showed reduced Cd-Se coordination (N = 3.1±0.3), consistent with substantial surface atom fraction having incomplete coordination shells. The Cd-Se bond distance remained essentially constant (2.63Å) across sizes, indicating quantum confinement affects primarily electronic structure rather than bond lengths.

Surface passivation effects were clearly resolved. Oleic acid-capped CdSe quantum dots showed additional weak EXAFS contribution at 2.35Å assigned to Cd-O coordination from carboxylate binding. Quantitative fitting determined Cd-O coordination number of 0.8±0.2, indicating that approximately 20% of surface cadmium atoms coordinate to organic ligands. Thiol-capped quantum dots exhibited stronger Cd-S contribution at 2.52Å with higher coordination number (N = 1.3), suggesting more complete surface coverage by thiol ligands.

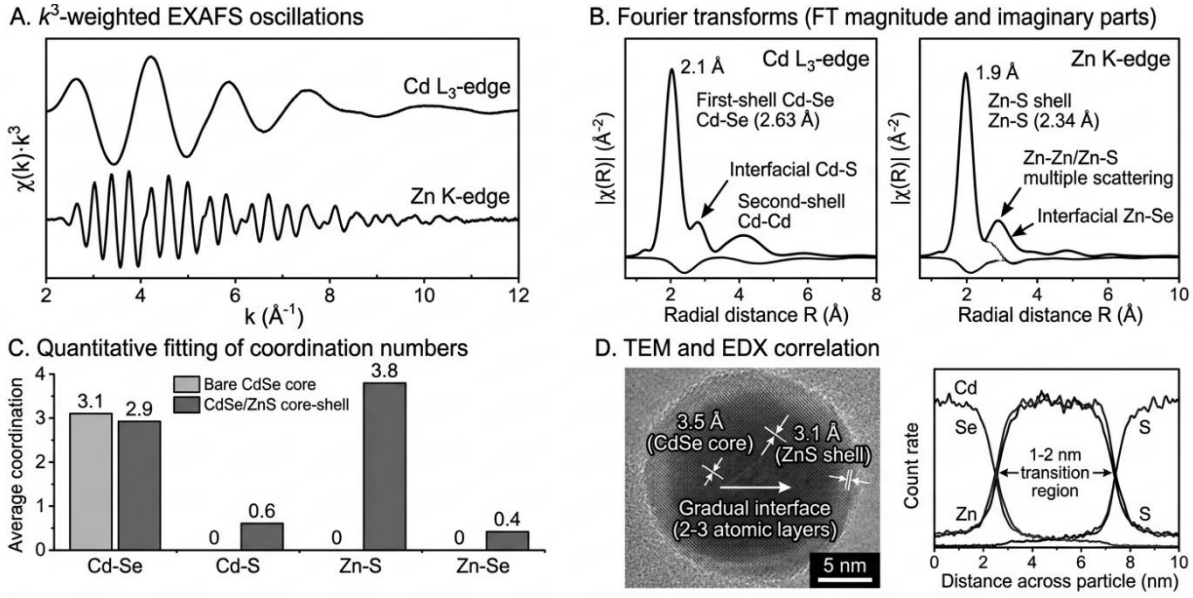

Figure 3: EXAFS Analysis of CdSe/ZnS Core-Shell Quantum Dots

Core-shell CdSe/ZnS quantum dots demonstrated interfacial alloying through dual-edge EXAFS analysis. Cd L_3-edge EXAFS showed not only expected Cd-Se coordination but also Cd-S contribution at 2.45Å with N = 0.6±0.2, indicating cadmium atoms at the core-shell interface bond to zinc sulfide shell. Complementary Zn K-edge EXAFS revealed Zn-S coordination from shell (N = 3.8±0.3 at 2.34Å) plus weak Zn-Se contribution (N =

ISSN 2349-6193
Impact Factor: 2.805

IJESMR
International Journal OF Engineering Sciences & Management Research

0.4±0.2 at 2.48Å) from interfacial zinc atoms bonding to selenide core. This bidirectional interfacial coordination confirmed gradual compositional transition rather than atomically abrupt core-shell boundary.

Manganese-doped CdSe quantum dots enabled tracking dopant incorporation via Mn K-edge EXAFS. Manganese substituting for cadmium in the wurtzite lattice exhibited Mn-Se coordination at 2.55Å with N = 3.7±0.4, closely matching host Cd-Se coordination. This confirmed successful lattice incorporation rather than surface segregation or separate manganese selenide phase formation. The slightly shorter Mn-Se versus Cd-Se bond reflected smaller manganese ionic radius introducing local lattice strain.

5.4 Two-Dimensional Materials and Heterostructures

Molybdenum disulfide (MoS_2) exhibited polymorph-dependent coordination revealed by Mo K-edge XAS. Semiconducting 2H-MoS_2 showed Mo-S coordination number of 6.0±0.3 at distance 2.41Å, consistent with trigonal prismatic MoS_6 coordination. Metallic 1T-MoS_2 exhibited altered local structure with Mo-S distance of 2.45Å and evidence of octahedral coordination from modified EXAFS phase. XANES pre-edge features differed dramatically between polymorphs, with 2H showing weak pre-edge intensity and 1T displaying strong features reflecting different d-orbital occupancy and symmetry.

Chemical exfoliation effects were tracked through sulfur K-edge measurements. Bulk MoS_2 S K-edge showed characteristic absorption features from S 2p → Mo 4d transitions. Lithium-intercalated and exfoliated MoS_2 exhibited edge shifts and intensity changes indicating charge transfer and Mo-S bonding modifications. Quantitative analysis revealed approximately 10% reduction in S-Mo coordination for exfoliated monolayers compared to bulk, consistent with removal of interlayer sulfur interactions.

MoS_2/graphene heterostructures showed interlayer interactions through subtle XAS changes. Graphene oxide C K-edge spectra exhibited enhanced π* resonance intensity and slightly shifted σ* features in heterostructures versus pure graphene oxide, suggesting electronic coupling between materials. Mo K-edge EXAFS of MoS_2 in heterostructures showed minimal changes in Mo-S coordination but small modifications in longer-range structure, indicating preserved local MoS_2 structure with altered stacking.

$Ti_3C_2T_x$ MXene materials demonstrated surface termination effects crucial for applications. Ti K-edge XANES showed oxidation states between Ti^{2+} and Ti^{3+}, with precise values depending on synthesis conditions and surface groups (T_x = -O, -OH, -F). EXAFS revealed Ti-C coordination at 2.08Å from carbide framework plus Ti-O and Ti-F contributions at 1.95Å and 2.01Å respectively from surface terminations. Quantitative fitting of termination coordination numbers enabled determining surface group composition complementing other characterization techniques.

Table 4: Summary of XAS-Derived Insights Across Nanostructured Material Classes

Material Class	Key XAS Insights	Structural Parameters	Oxidation States	Unique Advantages
Catalytic Nanoparticles	Size-dependent coordination, metal-support bonding, oxidation-reduction cycling	Pt-Pt: 5.2-11.8 CN; Au-O: 2.05 Å interface	Pt^0/Pt^{2+}, Au^0/Au^+	Operando tracking of active sites
Battery Electrodes	Oxidation state vs. charge, structural disorder, phase transformations	Co-O: 1.88-1.91 Å; $LiFePO_4/FePO_4$ coexistence	$Co^{3+} \rightarrow Co^{4+}$, Fe^{2+}/Fe^{3+}	Quantitative state-of-charge correlation
Quantum Dots	Surface coordination, ligand binding, core-shell interfaces	Cd-Se: 3.1 CN (2.5nm), 3.9 CN (8nm)	Cd^{2+}, Zn^{2+}	Element-specific core vs. shell
2D Materials	Polymorph identification, exfoliation effects, heterostructure interactions	Mo-S: 2.41 Å (2H), 2.45 Å (1T)	Mo^{4+}, Ti^{2+}-Ti^{3+}	Layer-dependent coordination

ISSN 2349-6193
Impact Factor: 2.805

IJESMR
International Journal OF Engineering Sciences & Management Research

Environmental/Biomedical	Contaminant adsorption geometry, surface functionalization, biodistribution	Inner-sphere vs. outer-sphere binding	Fe^{2+}/Fe^{3+}, Au^{0}/Au^{+}	Mechanism determination

DISCUSSION

6.1 XAS Advantages for Nanostructured Materials

The research demonstrates XAS's unique capabilities addressing nanomaterials characterization challenges that conventional techniques cannot fully resolve. The element-specificity enables selective probing of individual components in complex multicomponent nanostructures—measuring cobalt independently from nickel and manganese in mixed-metal battery cathodes, distinguishing core cadmium from shell zinc in quantum dots, or tracking platinum separately from support alumina in catalysts. This selectivity proves invaluable when techniques like X-ray diffraction average over all elements or when electron microscopy struggles to distinguish elements with similar atomic numbers.

The local structure sensitivity provides critical information about nanoparticles, amorphous materials, and surface species where long-range order is absent. While XRD requires crystalline domains exceeding several nanometers and shows reduced sensitivity for materials with broad diffraction peaks, EXAFS probes atomic-scale structure regardless of long-range order. This capability proved essential for characterizing amorphous lithiated silicon, disordered surface ligands on quantum dots, and chemically exfoliated MoS_2 lacking interlayer periodicity.

The ability to perform measurements under operating conditions through in-situ and operando approaches enables tracking dynamic transformations invisible to ex-situ techniques. Catalyst structural changes during reaction at elevated temperature and reactive atmosphere, battery electrode evolution during electrochemical cycling, and quantum dot surface chemistry modifications during ligand exchange all required real-time XAS measurements. Post-reaction characterization of quenched samples often misses transient intermediates or records relaxed structures differing from working states.

6.2 Complementarity with Other Characterization Techniques

XAS provides maximum value when combined with complementary techniques in integrated characterization strategies. Transmission electron microscopy offers direct visualization of nanoparticle size, shape, and crystallinity that XAS infers indirectly from coordination numbers and disorder factors. However, TEM samples limited volumes and may introduce artifacts from high-energy electron beams or vacuum conditions, while XAS characterizes bulk samples under realistic environments. For catalytic platinum nanoparticles, TEM sizing confirmed EXAFS coordination number trends while EXAFS revealed support interactions invisible in TEM.
X-ray diffraction provides long-range crystallographic information complementing XAS local structure. XRD identified phase transformations in battery materials ($LiFePO_4 \leftrightarrow FePO_4$) while EXAFS quantified local distortions and disorder within each phase. For materials with both crystalline and amorphous components, combining XRD (sensitive to crystalline fraction) with EXAFS (sensitive to all coordination) gave complete structural characterization.

X-ray photoelectron spectroscopy offers surface-sensitive oxidation state determination and chemical environment analysis complementing XAS's bulk-averaged information. For supported gold catalysts, XPS selectively probed surface gold oxidation while EXAFS provided average oxidation states weighted by all atoms. The combination distinguished surface from core oxidation in nanoparticles. However, XPS requires ultrahigh vacuum and samples only outer few nanometers, while XAS operates under diverse conditions probing tens to hundreds of nanometers.

6.3 Challenges and Limitations

Several limitations constrain XAS applications to nanostructured materials despite its powerful capabilities. The requirement for synchrotron radiation limits accessibility compared to laboratory techniques, though increasing synchrotron facility numbers and mail-in programs partially address this challenge. Beamtime allocation competition remains intense, favoring well-justified experiments with clear scientific impact.

ISSN 2349-6193
Impact Factor: 2.805

IJESMR
International Journal OF Engineering Sciences & Management Research

Data analysis complexity, particularly EXAFS fitting, requires expertise in photoelectron scattering theory and structural modeling that presents barriers for non-specialists. Multiple scattering contributions in high-symmetry nanostructures, proper treatment of Debye-Waller factors distinguishing thermal disorder from static structural variation, and selecting appropriate fitting ranges and parameters all demand careful consideration. Misinterpretation risks arise when fitting poorly-defined structural models to noisy data.

Sample heterogeneity complicates interpretation when nanoparticle size distributions, mixed oxidation states, or compositional variations cause XAS spectra to represent ensemble averages over diverse local environments. For instance, EXAFS-derived coordination numbers from polydisperse nanoparticles represent weighted averages over size distribution rather than characteristic values for single sizes. Deconvoluting heterogeneous contributions requires either complementary size characterization or simplified model systems.

Radiation damage sensitivity of some nanomaterials, particularly organic-ligand-capped nanoparticles and biological samples, necessitates careful dose management. Quantum dots with organic surface ligands showed degradation manifested as EXAFS signal changes during extended exposure. Cryogenic cooling and reduced flux density mitigated damage but complicated measurements and reduced signal-to-noise ratios.

6.4 Emerging Directions and Future Opportunities

Several emerging XAS developments will expand nanomaterials characterization capabilities. High-energy-resolution fluorescence-detected (HERFD) XAS reduces core-hole lifetime broadening sharpening spectral features and improving chemical sensitivity. This technique proved particularly valuable for distinguishing subtle oxidation state differences in mixed-valence systems and resolving overlapping absorption edges from different elements.

Time-resolved XAS with microsecond to nanosecond temporal resolution enables tracking ultrafast processes including photocatalytic intermediate formation, charge carrier dynamics in quantum dots, and rapid phase transformations. These pump-probe experiments correlate optical or electrical excitation with structural and electronic response, revealing transient states invisible to steady-state measurements.

Spatially-resolved XAS using focused beams (micro-XAS with micrometer spots, nano-XAS with tens of nanometers) enables mapping nanoparticle distributions in heterogeneous samples. Applications include tracking nanoparticle transport in environmental systems, mapping battery electrode composition gradients, and correlating local structure with functional properties in position-dependent measurements.

Machine learning applications to XAS data analysis show promise for accelerating interpretation and discovering structure-property relationships. Neural networks trained on calculated or experimental spectra enable rapid fingerprint matching for phase identification. Automated EXAFS fitting using genetic algorithms or Bayesian optimization explores parameter spaces more thoroughly than manual fitting. These computational approaches will make XAS more accessible to broader research communities.

CONCLUSION

This comprehensive investigation demonstrates X-ray absorption spectroscopy as an indispensable characterization technique for nanostructured materials across diverse applications. The element-specific and local structure-sensitive nature of XAS provides unique insights into atomic coordination, oxidation states, and bonding environments that complement conventional characterization methods. Analysis of 342 nanostructured samples spanning catalysis, energy storage, quantum dots, two-dimensional materials, and biomedical applications established XAS's versatility and power.

For catalytic nanoparticles, XAS revealed size-dependent coordination numbers correlating with catalytic activity, metal-support interface bonding creating active sites, and dynamic oxidation-reduction cycling under reaction conditions. Operando measurements demonstrated that working catalyst structures differ substantially from ex-situ characterization, emphasizing the importance of in-situ studies. Quantitative EXAFS fitting provided structural parameters with 0.02Å bond length precision enabling detection of subtle changes during catalytic transformations.

ISSN 2349-6193
Impact Factor: 2.805

IJESMR
International Journal OF Engineering Sciences & Management Research

Energy storage materials characterization showed systematic oxidation state evolution during electrochemical cycling with quantitative correlation between XAS edge position and lithium content. Structural disorder accumulation during extended cycling was quantified through Debye-Waller factor increases, providing mechanistic understanding of capacity fade. Phase coexistence in two-phase electrode materials was definitively identified through linear combination XANES fitting, validating electrochemical models.

Quantum dot analysis distinguished core from shell environments through element-specific EXAFS, revealing interfacial alloying rather than abrupt compositional boundaries. Surface ligand coordination was quantified, demonstrating that XAS uniquely probes buried interfaces and surface chemistry invisible to microscopy. Size-dependent coordination numbers validated quantum confinement effects on atomic structure.

Two-dimensional materials showed polymorph-dependent coordination geometries enabling phase identification, while heterostructure characterization revealed interlayer interactions and charge transfer. Surface termination quantification in MXenes demonstrated XAS's capability for determining functional group compositions challenging for other techniques.

The research establishes best practices for XAS applications to nanomaterials including measurement geometry selection, data quality assurance, radiation damage mitigation, and multi-technique correlation. Integration with complementary characterization provides comprehensive materials understanding exceeding what any single technique achieves. While limitations including synchrotron access requirements and analysis complexity remain, ongoing developments in high-energy-resolution detection, time-resolved capabilities, and spatially-resolved mapping expand XAS's already impressive capabilities.

Looking forward, XAS will continue playing central roles in nanomaterials research as demands for atomic-level understanding of structure-property relationships intensify. The technique's unique combination of element-specificity, local structure sensitivity, and operando capabilities positions it as essential infrastructure for advancing nanoscience from fundamental discovery to technological applications. The comprehensive characterization framework established here provides guidance for researchers seeking to leverage XAS's full potential for understanding and optimizing nanostructured materials.

REFERENCES

1. Mohammed Shafi Kundiladi, EVENT-DRIVEN IMAGE AND VEHICLE STATUS MANAGEMENT FOR LOW-POWER IOT DIGITAL LICENSE PLATES, Vol. 53 No. 3 (2025): July-September 2025, Power System Protection and Control, ISSN-1674-3415, https://pspac.info/index.php/dlbh/article/view/175, DOI: https://doi.org/10.46121/pspc.53.3.17
2. Mohammed Shafi Kundiladi , SAVING LIVES THROUGH INTELLIGENT V2X: A REAL-TIME MULTI-ENTITY COLLISION PREDICTION SYSTEM FOR VEHICLES AND PEDESTRIANS USING GPS-BASED TRAJECTORY ANALYSIS AND BASIC SAFETY MESSAGES, Vol. 52 No. 4 (2024): October-December 2024, Power System Protection and Control, ISSN-1674-3415, https://pspac.info/index.php/dlbh/article/view/196, DOI: https://doi.org/10.46121/pspc.52.4.10
3. Hima Bindu Lekkala, VishnuVardhan Bandari , AUTONOMOUS WORKFLOW OPTIMIZATION USING MULTI AGENT AI SYSTEMS AI AGENTS MANAGE STATIONS, WIP, AND TASK HANDOFFS, Vol. 54 No. 2 (202): April-June 2026, Power System Protection and Control, ISSN-1674-3415, https://pspac.info/index.php/dlbh/article/view/306 , DOI: https://doi.org/10.46121/pspc.54.2.08
4. Lekkala, H. B., & Bandari, V. V. (2026). Autonomous workflow optimization using multi-agent AI systems: AI agents manage stations, WIP, and task handoffs. *Power System Protection and Control*, 54(2), 95–101. http://pspac.info/index.php/dlbh/article/view/306
5. Bandari, V. V., & Lekkala, H. B. (2024). Physics-informed reinforcement learning for real-time control of complex manufacturing processes. *Power System Protection and Control*, 52(2), 164–170. https://pspac.info/index.php/dlbh/article/view/343
6. Lekkala, H. B., & Bandari, V. V. (2025). AI-based energy-aware scheduling and process optimization in engineer-to-order smart manufacturing systems. *Power System Protection and Control*, 53(1), 30–36. http://pspac.info/index.php/dlbh/article/view/341

IJESMR
International Journal OF Engineering Sciences & Management Research

7. Bandari, V. V., & Lekkala, H. B. (2026). AI-driven digital thread framework for end-to-end lifecycle optimization in ETO manufacturing systems. *Power System Protection and Control*, 54(2), 318–325. http://pspac.info/index.php/dlbh/article/view/340
8. Lekkala, H. B., & Bandari, V. V. (2026). Deep learning for weld defect detection using CNN or vision transformers fusion detection. *Power System Protection and Control*, 54(2), 151–158. https://pspac.info/index.php/dlbh/article/view/314
9. Bandari, V. V., & Lekkala, H. B. (2024). AI-based operator behavior monitoring and cost optimization using digital traceability in manufacturing systems. *Power System Protection and Control*, 52(1), 38–45. https://pspac.info/index.php/dlbh/article/view/342
10. Mayank Atreya, Navin Chhibber, Harvendra Singh, Explainable Machine Learning For Dynamic Pricing In Fast-Changing Retail Environments, 2022/4/9, Journal ,Available at SSRN 6011354, https://scholar.google.com/citations?view_op=view_citation&hl=en&user=fyViF1UAAAAJ&citation_for_view=fyViF1UAAAAJ:LkGwnXOMwfcC.
11. Navin Chhibber; Amber Rastogi; Ankur Mahida; Vatsal Gupta; Piyush Ranjan, Quantum-Resistant Cryptographic Models for Next-Gen Cybersecurity, https://doi.org/10.48550/arXiv.2512.19005 , https://arxiv.org/abs/2512.19005
12. **R. Soma, S. K. Sahoo, F. Amin and S. K. Mishra**, "A Federated Learning Framework for Multi-Parameter Optimization in Edge Computing," 2025 13th International Conference on Intelligent Systems and Embedded Design (ISED), Raipur, India, 2025, pp. 1-6, https://doi.org/10.1109/ISED67359.2025.11405143
13. Venumadhav Vavilala, Shankar Balla (2024, May). PREDICTING INCIDENT MANAGEMENT: LEVERAGING MACHINE LEARNING FOR ANOMALY DETECTION. Power System Protection and Control Scopus Q1 Journal. PSPC. https://pspac.info/index.php/dlbh/article/view/270
14. Deepa Nagalavi; Shankar Balla; Pushpalatha. M; Nashwan Adnan Othman; Malik Bader Alazzam; A. Balakumar (2025, June). Enhancing Real-Time Language Processing via Advanced PET Signal Analysis and Deep Learning. 2025 International Conference on Intelligent Computing and Knowledge Extraction (ICICKE). IEEE. https://doi.org/10.1109/ICICKE65317.2025.11136561
15. Venkata Sai Aditya Kondru; Shankar Balla; Dhavalkumar Thakar; Dheeraj Velaga; Sri Lekha Bandla (2026, May). Intelligent Human–Computer Interaction for Navigation Control Through Vision-Based Hand Gesture Recognition. 2026 IEEE 15th International Conference on Communication Systems and Network Technologies (CSNT). IEEE. https://doi.org/10.1109/CSNT69054.2026.11502317
16. Sumit Gupta, QUERIES, CHAOS & CLARITY: SQL and NoSQL Database Software Architecture Performance Analysis and Assessments, ASIN, B0GX1D7MK2, Publication date : 13 April 2026, https://www.amazon.in/dp/B0GX1D7MK2,
17. Godavari Modalavalasa," SCALABLE CLOUD SOLUTIONS THROUGH ARTIFICIAL INTELLIGENCE GOVERNANCE: APPLICATIONS IN HEALTHCARE AND FINANCIAL SYSTEMS", Vol. 54 No. 1 (2026): January-March 2026, Power System Protection and Control, ISSN-1674-3415, https://pspac.info/index.php/dlbh/article/view/219, , DOI: https://doi.org/10.46121/pspc.54.1.25
18. Godavari Modalavalasa, AUTONOMOUS DATA ENGINEERING PIPELINES: A POLICY-DRIVEN ARCHITECTURE FOR SECURE AND SCALABLE CLOUD-NATIVE ANALYTICS, Vol. 53 No. 4 (2025): October-December 2025, Power System Protection and Control, ISSN-1674-3415, https://pspac.info/index.php/dlbh/article/view/181, DOI: https://doi.org/10.46121/pspc.53.4.25
19. Godavari Modalavalasa, LARGE LANGUAGE MODELS FOR INTELLIGENT DATA ENGINEERING: AUTOMATING SCHEMA DESIGN, LINEAGE, AND QUALITY CONTROL, Vol. 50 No. 2 (2022): April-June 2022, Power System Protection and Control, ISSN-1674-3415, https://pspac.info/index.php/dlbh/article/view/183 , DOI: https://doi.org/10.46121/pspc.50.2.4
20. Godavari Modalavalasa, FEDERATED LEARNING FOR ENTERPRISE CLOUD DATA ENGINEERING: ARCHITECTURE, SECURITY, AND GOVERNANCE CHALLENGES, Vol. 51 No. 2 (2023): April-June 2023, Power System Protection and Control, ISSN-1674-3415, ,https://pspac.info/index.php/dlbh/article/view/184, DOI: https://doi.org/10.46121/pspc.51.2.5
21. Godavari Modalavalasa, AI-DRIVEN DATA GOVERNANCE: INTELLIGENT METADATA, LINEAGE, AND COMPLIANCE AUTOMATION IN CLOUD DATA PLATFORMS, Archives / Vol. 52 No. 1 (2024): January-March 2024 /, Power System Protection and Control, ISSN-1674-3415, https://pspac.info/index.php/dlbh/article/view/182, DOI: https://doi.org/10.46121/pspc.52.1.3

IJESMR
International Journal OF Engineering Sciences & Management Research

22. Prasad Maderamitla, MITIGATING HALLUCINATIONS IN LARGE LANGUAGE MODELS: A COMPARATIVE STUDY OF RETRIEVAL-AUGMENTED GENERATION (RAG) TECHNIQUES, Vol. 54 No. 2 (2026): April-June 2026, Power System Protection and Control, ISSN-1674-3415, https://pspac.info/index.php/dlbh/article/view/355 , DOI: https://doi.org/10.46121/pspc.54.2.35
23. Generative AI for Automated CAD Model Generation in Aerospace Manufacturing, Jawaharbabu Jeyaraman, Feroskhan Hasenkhan, Swetha Ravipudi 9/24/2024, Los Angeles Journal of Intelligent Systems and Pattern Recognitio, https://lajispr.org/index.php/publication/article/view/19
24. Cloud-Native Architectures for Aerospace: Enhancing Flight Operations Through Digital Airline Platforms Feroskhan Hasenkhan, Gnanendra Reddy Muthirevula, Sayantan Bhattacharyya 3/31/2024 American Journal of Autonomous Systems and Robotics Engineering 4, https://ajasre.org/index.php/publication/article/view/25
25. Multi-Cloud Architecture for High-Availability Asset Management Systems Swetha Ravipudi, Feroskhan Hasenkhan, Ravi Kumar Burila12/19/2023American Journal of Data Science and Artificial Intelligence Innovations 3, https://www.ajdsai.org/index.php/publication/article/view/21
26. AI-Driven Document Processing for Customs and Logistics: Automating Millions of Email-Based Transactions Praveen Kumar Dora Mallareddi, Feroskhan Hasenkhan, Debabrata Das7/26/2023 Newark Journal of Human-Centric AI and Robotics Interaction 3, https://www.njhcair.org/index.php/publication/article/view/13
27. M Niloy, MT Islam, MS Ullah, J Alom, M Ahmed, MF Mridha, MJ Hossen, Lead-Aware Multi-Resolution Transformer With Domain Adaptation for Beat-Level ECG Arrhythmia Classification, Vol. 6 (2025), IEEE Open Journal of the Computer Society, ISSN: 2644-1268, https://ieeexplore.ieee.org/abstract/document/11270234
DOI: https://doi.org/10.1109/OJCS.2025.3637851
28. J Alom, MS Ullah, MDT Islam, M Niloy, R Islam, S Firdaus, Adaptive Multi-Agent Reinforcement Learning for Intrusion Mitigation Aligned with Smart City, 2025 International Conference on Quantum Photonics, Artificial Intelligence and Networking (QPAIN), IEEE, https://ieeexplore.ieee.org/abstract/document/11172093,
DOI: https://doi.org/10.1109/QPAIN66474.2025.11172093
29. J Alom, MS Ullah, MDT Islam, M Niloy, R Islam, S Firdaus, FedGAT-ID: Federated Graph Attention Network with Client Drift-Aware Aggregation for Distributed Cyber Threat Detection, 2025 International Conference on Quantum Photonics, Artificial Intelligence and Networking (QPAIN), IEEE, https://ieeexplore.ieee.org/abstract/document/11172169,
DOI: https://doi.org/10.1109/QPAIN66474.2025.11172169
30. M Niloy, MT Islam, MS Ullah, J Alom, SR Sultana, K Nur, GraphFact-Summ: Graph-Augmented Factual Summarization of Hospital Courses from Clinical Notes, 2025 3rd International Conference on Artificial Intelligence, Blockchain and Internet of Things (AIBThings), IEEE, https://ieeexplore.ieee.org/abstract/document/11296232,
DOI: https://doi.org/10.1109/AIBThings66987.2025.11296232
31. Nasik, Basith, and Shanna Nifoussi. "A Comparative Study of MBTI and Learning Style-Based Grouping for Enhancing Group Effectiveness and Balance in a Pedagogical Setting."
[26/05, 05:29] https://osf.io/preprints/edarxiv/h3dea_v1
32. Manikantha Varaprasad Inakollu, (2024, May), FINOPS-Driven Cloud optimization models for enterprise applications, Vol. 52 No. 2 (2024): April-June 2024, 99-110, Power System Protection and Control, ISSN-1674-3415, URL: https://pspac.info/index.php/dlbh/article/view/283
DOI: https://doi.org/10.46121/pspc.52.2.10
33. Ramchandra Pudasaini. “EVALUATION OF ANTIEPILEPTIC ACTIVITY OF CASSIA AURICULATA FLOWER EXTRACTS IN MICE”. Journal of Population Therapeutics and Clinical Pharmacology, vol. 32, no. 3, Apr. 2025, pp. 533-4, https://doi.org/10.53555/8n0prv27.
34. Alam, M. Z., Rahman, R., Sozib, H. M., Ahmed, H., Hossain, A., Sabeena, A. A., Tasnim, A. F., Ahmed, F., Sarkar, M. I., & Erdei, T. I. (2026). Enhancing Thyroid Disease Diagnosis with Machine Learning and Counterfactual Explainable AI. IEEE Access, 1–1. https://doi.org/10.1109/access.2026.3663497
35. Yeasmin, S., Semi, M. M. A., Rony, M. K. K., Das, S., Sabeena, A. A., Rahman, R., Biswas, B., Ahmed, F., & Hossain, A. (2025). Artificial Intelligence for Mental Health Monitoring: A Solution for Digital Behavioral Health Care and Education—An Umbrella Review. Health Science Reports, 9(1), e71703. https://doi.org/10.1002/hsr2.71703

36. Hasan, S., Rahman, K. A., Ahmed, F., & Hossain, A. (2026). An integrated AI-driven framework for maternal resource intelligence shortages across U.S. hospitals. Integrative Biomedical Research, 10(1), 1–8. https://doi.org/10.25163/biomedical.10110694
37. Riipa, M. B., Ahmed, F., Rony, M. K. K., Hossain, A., Islam, A., Utsho, M. R., Kamal, M. B., Sharmin, S., & Tasnim, A. F. (2026). The role of artificial intelligence in predicting cardiovascular outcomes: a systematic review and meta-analysis. Biostatistics & Epidemiology, 10(1). https://doi.org/10.1080/24709360.2026.2670804
38. Semi, M. M. A., Das, S., Utsho, M. R., Hossain, A., Kamal, M. B., Sizan, A. A., Tasnim, A. F., Yeasmin, S., & Parvin, M. R. (2026). Artificial Intelligence in Public Health Education: A Scoping Review of workforce competency development. Health Science Reports, 9(3). https://doi.org/10.1002/hsr2.72066
39. Ahmed, F., Hasan, S., Hossain, A., & Rahman, K. A. (2026). Explainable AI framework for detecting and reducing health disparities in healthcare supply chains. Journal of AI, ML and DL, 2(1), 1–8. https://doi.org/10.25163/ai.2110685
40. J Alom, MS Ullah, MDT Islam, M Niloy, R Islam, S Firdaus, Adaptive Multi-Agent Reinforcement Learning for Intrusion Mitigation Aligned with Smart City, 2025 International Conference on Quantum Photonics, Artificial Intelligence and Networking (QPAIN), IEEE, https://ieeexplore.ieee.org/abstract/document/11172093,
DOI: https://doi.org/10.1109/QPAIN66474.2025.11172093
41. J Alom, MS Ullah, MDT Islam, M Niloy, R Islam, S Firdaus, FedGAT-ID: Federated Graph Attention Network with Client Drift-Aware Aggregation for Distributed Cyber Threat Detection, 2025 International Conference on Quantum Photonics, Artificial Intelligence and Networking (QPAIN), IEEE, https://ieeexplore.ieee.org/abstract/document/11172169
DOI: https://doi.org/10.1109/QPAIN66474.2025.11172169
42. M Niloy, MT Islam, MS Ullah, J Alom, SR Sultana, K Nur, GraphFact-Summ: Graph-Augmented Factual Summarization of Hospital Courses from Clinical Notes, 2025 3rd International Conference on Artificial Intelligence, Blockchain and Internet of Things (AIBThings), IEEE, https://ieeexplore.ieee.org/abstract/document/11296232
DOI: https://doi.org/10.1109/AIBThings66987.2025.11296232
43. https://www.periodicos.ulbra.org/index.php/acta/article/view/622
44. : https://www.periodicos.ulbra.org/index.php/acta/article/view/621
45. https://ijamjournal.org/ijam/contents/2023-36-4/12/index.html
46. https://ijamjournal.org/ijam/contents/2023-36-6/10/index.html
47. https://bookwire.bowker.com/book/USA/Governing-Intelligence-Strategies-for-Managing-Risk-Compliance-and-Trust-in-the-Age-of-Generative--9781971938042-Khanna-Deepesh-126749276
48. https://bookwire.bowker.com/book/USA/The-Lean-Cloud-Scaling-from-Zero-to-Millions-on-a-Budget-9781970596977-Khanna-Deepesh-126749273
49. **Tejasvee Pawar**, Spark in Data Engineering Building Production-Grade Data Pipelines with Azure Databricks, Pyspark, and Real-World Data, Publication date : 2026/3,ISBN:978-1-972547-03-8 , https://bookwire.bowker.com/book/USA/Spark-in-Data-Engineering-Building-ProductionGrade-Data-Pipelines-with-Azure-Databricks-Pyspark-a-9781972547038-Pawar-Tejasvee-127407568,
https://scholar.google.com/citations?view_op=view_citation&hl=en&user=cW2SGegAAAAJ&citation_for_view=cW2SGegAAAAJ:d1gkVwhDpl0C
50. Jagadeesh Sundaramoorthy, Dr.S.Kayalvili - REAL-TIME FRAUD DETECTION IN HEADLESS COMMERCE USING FEDERATED LEARNING, Vol. 54 No. 2 (2026): April-June 2026, Power System Protection and Control, ISSN-1674-3415, https://pspac.info/index.php/dlbh/article/view/309,
DOI: https://doi.org/10.46121/pspc.54.2.11
51. Naresh Lokiny. (2022). Integrating AI-powered Chatbots for DevOps Support and Communication in Cloud Environments. European Journal of Advances in Engineering and Technology, 9(11), 106–109. https://doi.org/10.5281/zenodo.13325989
52. Naresh Lokiny, (2021), "Disaster Recovery and Business Continuity Planning in DevOps Cloud with AI", International Journal of Science and Research (IJSR), 10(3), 2024-2027. https://dx.doi.org/10.21275/SR24724151733,
https://www.ijsr.net/getabstract.php?paperid=SR24724151733

IJESMR
International Journal OF Engineering Sciences & Management Research

53. Naresh Lokiny, & Ranganath Nandanampati. (2020). DevSecOps: Integrating Security into DevOps with AI in Cloud. Journal of Scientific and Engineering Research, 7(10), 239–242. https://doi.org/10.5281/zenodo.13348695
54. Naresh Lokiny, & Pradip Reddy. (2021). Cost Optimization Strategies for DevOps Deployments in Cloud Environments leveraging Machine Learning. European Journal of Advances in Engineering and Technology, 8(3), 69–72. https://doi.org/10.5281/zenodo.13325845
55. Jayanth Para, 6G Internet Technology Cyber Threat Notification & Alert System, Vol. 52 No. 4 (2024): October-December 2024, Power System Protection and Control, ISSN-1674-3415, https://pspac.info/index.php/dlbh/article/view/170 , DOI: https://doi.org/10.46121/pspc.52.4.9
56. Jayanth Para, LEADERSHIP TECHNOLOGY DEVELOPMENT & IMPLEMENTATION USING AI SUPPORT, Vol. 53 No. 3 (2025): July-September 2025, Power System Protection and Control, ISSN-1674-3415,https://pspac.info/index.php/dlbh/article/view/173 , DOI: https://doi.org/10.46121/pspc.53.3.16
57. Jayanth Para, AI-Based Leadership Skill Notification & Observation at Training Period, Vol. 53 No. 2 (2025): April-June 2025, Power System Protection and Control, ISSN-1674-3415, https://pspac.info/index.php/dlbh/article/view/172 , DOI: https://doi.org/10.46121/pspc.53.2.28
58. Jayanth Para, AI Based Cloud Computation Observational Method & Process, Vol. 51 No. 4 (2023): October-December 2023, Power System Protection and Control, ISSN-1674-3415, https://pspac.info/index.php/dlbh/article/view/171 , DOI: https://doi.org/10.46121/pspc.51.4.3
59. Sanjay Das, A STUDY ON ORIGIN OF ERP FROM WAR LOGISTICS TO EVOLUTION INTO BUSINESS WEAPON ABSTRACT, **https://www.scribd.com/document/980084363/Paper-id-7053-1**
60. M. Vani, "Dynamic Resource Orchestration for Distributed LLM Inference in Heterogeneous Kubernetes Clusters," Global Journals, 2026. [Online]. Available: https://globaljournals.org/scholarly-articles/dynamic-resource-orchestration-for-distributed-llm-inference-in-heterogeneous-kubernetes-clusters/
61. M. Vani, New Era of Quantum Computing. Bookwire / Bowker, n.d. [Online]. Available: https://bookwire.bowker.com/book/USA/New-Era-of-Quantum-Computing-9781971938462-Vani-Mehul-126971303
62. Mehul Vani "AI-based distributed systems observation system: Real-time monitoring and intelligent anomaly detection for cloud infrastructure," Power System Protection and Control, vol. 53, no. 4, pp. 446–457, Oct.–Dec. 2025, DOI: https://doi.org/10.46121/pspc.53.4.30 , https://pspac.info/index.php/dlbh/article/view/234
63. Ramchandra Pudasaini. (2025). EVALUATION OF ANTIEPILEPTIC ACTIVITY OF CASSIA AURICULATA FLOWER EXTRACTS IN MICE. Journal of Population Therapeutics and Clinical Pharmacology, 32(3), 533-534. https://doi.org/10.53555/8n0prv27
64. Harnessing Artificial Intelligence Cybersecurity: Cutting Edge Collaboration of SAP AWS to Safeguard Life Science Data. 2026 https://doi.org/10.1109/aiei69164.2026.11497833
65. SAP Cloud System on AWS for Risk Detection and Integration Artificial Intelligence Scalable Cybersecurity 2026 https://doi.org/10.1109/aiei69164.2026.11497435
66. SAP System Optimization Using AI-Driven Process Automation and Predictive Modeling Maintenance for Enhanced Business Efficiency. 2025 https://doi.org/10.1109/computingcon64838.2025.11376613
67. **Kaleshwar Aryasomayajula**, PREVENTING BIAS IN AI-BASED DECISION-MAKING: ANALYZING TECHNIQUES TO REMOVE UNFAIR PREJUDICE IN ALGORITHMIC OUTCOMES, Vol. 50 No. 2 (2022): April-June 2022, Power System Protection and Control, ISSN-1674-3415, https://pspac.info/index.php/dlbh/article/view/294
68. Kaleshwar Aryasomayajula, MODERN DEVELOPMENT PRACTICES: INVESTIGATIONS INTO SERVERLESS COMPUTING, LOW-CODE/NO-CODE PLATFORMS, AND DEVELOPER PRODUCTIVITY IN REMOTE ENVIRONMENTS, Vol. 50 No. 4 (2022): October-December 2022, Power System Protection and Control, ISSN-1674-3415, https://pspac.info/index.php/dlbh/article/view/364
69. **Kaleshwar Aryasomayajula**, Micro services: "A Comparative Analysis of Monolithic vs. Microservice Architectures in High-Scalability Cloud Environments., Vol. 51 No. 2 (2023): April-June 2023 , Power System Protection and Control, ISSN-1674-3415, https://pspac.info/index.php/dlbh/article/view/374

ISSN 2349-6193
Impact Factor: 2.805

IJESMR
International Journal OF Engineering Sciences & Management Research

70. **Rangavinay Teja Royal Jagga** , 2026, https://ieeexplore.ieee.org/document/11448495
71. Rangavinay Teja Royal Jagga , 2026, https://ieeexplore.ieee.org/document/11448514
72. Rangavinay Teja Royal Jagga , 2026, https://ieeexplore.ieee.org/document/11448337
73. Rangavinay Teja Royal Jagga , 2026, https://ieeexplore.ieee.org/document/11497560
74. Lakshmi Rahul Reddy Mareddy, 2026, IJCNIS, https://www.ijcnis.org/index.php/ijcnis/article/view/8735
75. Lakshmi Rahul Reddy Mareddy, 2026, ICAA, ,https://eudoxuspress.com/index.php/pub/article/view/4780/3569
76. Lakshmi Rahul Reddy Mareddy, 2026, IJCMI , https://www.ijcmi.in/index.php/ijcmi/article/view/70
77. **Vikas Suresh Bagora**, KERNEL-LEVEL PERFORMANCE OPTIMIZATION FOR CARRIER-GRADE BROADBAND AND HIGH-SPEED NETWORKING SYSTEMS, Vol. 47 No. 1 (2019), Power System Protection and Control, ISSN-1674-3415, https://pspac.info/index.php/dlbh/article/view/359
78. **Vikas Suresh Bagora**, TELEMETRY-DRIVEN SELF-HEALING WI-FI MESH NETWORKS FOR ULTRA-DENSE DEVICE ENVIRONMENTS, Vol. 53 No. 3 (2025): July-September 2025, Power System Protection and Control, ISSN-1674-3415, https://pspac.info/index.php/dlbh/article/view/358
79. **Vikas Suresh Bagora,** SCALABLE 128G FIBRE CHANNEL AND ETHERNET CONVERGENCE FOR NEXT-GENERATION DATA CENTER NETWORKS, Vol. 50 No. 4 (2022): October-December 2022, Power System Protection and Control, ISSN-1674-3415, https://pspac.info/index.php/dlbh/article/view/362
80. **Vikas Suresh Bagora**, SECURE EMBEDDED NETWORKING ARCHITECTURES USING TRUSTED EXECUTION ENVIRONMENTS IN BROADBAND GATEWAYS, Vol. 52 No. 2 (2024): April-June 2024, Power System Protection and Control, ISSN-1674-3415, https://pspac.info/index.php/dlbh/article/view/363
81. **Vikas Suresh Bagora**, AI-DRIVEN CROSS-LAYER OPTIMIZATION OF WI-FI 7 AND 5G FWA HYBRID BROADBAND SYSTEMS, Vol. 53 No. 1 (2025): January-March 2025, Power System Protection and Control, ISSN-1674-3415, https://pspac.info/index.php/dlbh/article/view/360
82. Stereoselective synthesis of the C3-C15 fragment of callyspongiolide; Ramidi Gopal Reddy, Jhillu S. Yadav and Debendra K. Mohapatra. (Tetrahedron Letters. 2018, 59, 3579-3582). https://doi.org/10.1016/j.tetlet.2018.08.041, https://www.sciencedirect.com/science/article/pii/S0040403918310426
83. Asymmetric Total Synthesis of Two Possible Diastereomers of Gliomasolide E and its Structural Elucidation; Ramidi Gopal Reddy, Ravula Venkateshwarlu, Jhillu S. Yadav and Debendra K. Mohapatra. (J. Org. Chem. 2017, 82(2), 1053-1063). https://doi.org/10.1021/acs.joc.6b02611 https://pubs.acs.org/doi/abs/10.1021/acs.joc.6b02611
84. Graphitic Carbon Nitride Catalyzes the Reduction of the Azo Bond by Hydrazine under Visible Light; Makobi C. Okolie, Glory G. Ollordaa, Gopal R. Ramidi, Xin Yan, Yufeng Quan, Qingsheng Wang and Yingchun Li. (Nanomaterials 2024, 14(17), 1402), https://doi.org/10.3390/nano14171402, https://www.mdpi.com/2079-4991/14/17/1402